Acta Materialia 297 (2025) 121330

Contents lists available at ScienceDirect

Acta Materialia

journal homepage: www.elsevier.com/locate/actamat

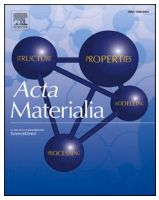

Full length article

Grain size effects on stress-assisted grain boundary migration in polycrystalline Au thin films under tension

Sandra Stangebye [a], Kunqing Ding [b], Yichen Yang [b], Ting Zhu [a,b], Olivier Pierron [b], Josh Kacher [a,*]

[a] School of Materials Science and Engineering, Georgia Institute of Technology, Atlanta, GA 30332, USA
[b] Woodruff School of Mechanical Engineering, Georgia Institute of Technology, Atlanta, GA 30332, USA

ARTICLE INFO

Keywords:
In situ electron microscopy
Grain boundary migration
Dislocations

ABSTRACT

Grain boundaries play an important role in the deformation of ultrafine-grained and nanocrystalline metals and are key to understanding and improving their mechanical properties. This study combines orientation mapping with *in situ* transmission electron microscopy straining at low applied strain rates to investigate the grain boundary migration behavior as a function of microstructure in both as-fabricated and annealed ultrafine grained Au specimens. The main observation for the unannealed specimens is that small grains are consistently removed upon straining. This increased grain boundary mobility near small grains is attributed to grain size-dependent yielding, leading to a strain energy difference across the grain boundary. Molecular dynamics simulations reveal a local smoothing effect arising from coupled sliding-migration at curved grain boundaries, which could be an additional cause for smaller grains to shrink. Other microstructural features such as grain boundary misorientation, grain orientation, and Schmid factor are investigated in the annealed specimens (when grain removal is scarce), but no clear correlations are found.

1. Introduction

Nanocrystalline (NC) and ultrafine-grained (UFG) metals exhibit superior strength compared to their coarse-grained counterparts due to the high-density of grain boundaries (GBs) that restrict dislocation glide [1]. However, they are also notorious for exhibiting low thermal/-mechanical stability due to an evolving GB network by the activation of GB-mediated mechanisms. A growing number of studies have shown that grain growth, which is typically considered to be a thermally-driven process, can be activated by mechanical loading in NC and UFG metals [2–6], even at room and cryogenic temperatures [7]. Some studies suggest that this grain growth is favorable as it facilitates a means for plastic deformation and can have a large impact on the mechanical properties. For example, Gianola et al. found that NC Al specimens show increased ductility if stress-assisted GB migration is activated compared to counterparts that experience no grain growth [2]. Additional studies have suggested that grain growth mediated by stress assisted grain boundary (GB) migration occurs prior to (and thus helps facilitate) transgranular dislocation activity. In situ TEM straining of NC Al has shown fast GB migration near a crack tip prior to dislocation activity [8], while other studies have shown that grain coarsening occurs in the immediate vicinity of an indenter tip during in situ TEM nano-indentation, with the coarsening halting once grains are large enough to accommodate dislocation activity [9]. Other studies suggest that grain growth can have a softening effect as the nano-sized grains are eliminated [10]. Mechanically-driven grain growth has been observed in a wide range of NC/UFG metals under different loading conditions, including uniaxial tension or compression [2,3,8,11,12], torsion [13,14], indentation [9,15], and cyclic loading [5,6,16–18]. The extent of grain growth has been shown to depend on the loading condition [17,19], is non-uniform across different grains [19], and depends on the local stress state (i.e. normal versus shear stress) [3]. Additional studies have suggested that grain growth behavior varies depending on the initial microstructure such as grain size and film texture [2,4,16,18,19]. Grain growth has been shown to occur via stress assisted GB migration and/or grain rotation [20,21], with GB migration usually considered to be the dominant mechanism [22]. Understanding the numerous factors that influence mechanically-induced grain GB is key to improving NC and UFG mechanical properties and stability.

GB kinetics dictate the evolution of a GB network and structure and

* Corresponding author.
E-mail address: josh.kacher@mse.gatech.edu (J. Kacher).

https://doi.org/10.1016/j.actamat.2025.121330
Received 14 March 2025; Received in revised form 11 July 2025; Accepted 11 July 2025
Available online 12 July 2025

are central to understanding how NC/UFG materials evolves during deformation. The fundamental kinetic equation used to describe GB migration is:

$$v_{\perp} = M_z F \quad (1)$$

where $v_{\perp}$ is GB migration velocity defined normal to GB plane, F is the applied driving force and M_z is the intrinsic GB mobility that relates $v_{\perp}$ to F [23]. The intrinsic mobility is an equilibrium GB property that depends on material parameters, temperature, and/or bi-crystallography and, in addition to the driving force, controls the evolution of grain morphology and crystallography [23]. Much of the research investigating the stress-based driving force involves either molecular dynamics (MD) simulations [24–27] or experiments [28–31] on bicrystals. Molodov et al. investigated the stress-driven motion of three Σ7 boundaries in Al as a function of GB angle/axis pair [31]. Their results indicate that crystallographically equivalent symmetric tilt GBs show different responses (migration rates) under an applied stress. Additional results indicate that GB mobility is related to GB structure with a generally accepted view that mobility increases for HAGB compare to LAGB [32,33]. Olmsted et al. also determined that GB mobility is not closely correlated with Σ value with the single exception of Σ3 boundaries [25]. MD simulations on a flat GB in an Al bicrystal have determined that the mobility of mixed-type boundaries is markedly higher than that of a pure twist or tilt boundary due to the increased disorder of mixed-type boundaries [33]. The simulations also showed that two GBs with the same misorientation angle-axis pair but different boundary planes can have very different mobilities, with increasing GB mobility correlating with increasing deviation of the GB plane from {111}.

The abovementioned bicrystal studies typically do not capture the behavior of GBs present in polycrystals that have additional restrictions, such as triple junction (TJ) and more complex stress states. Computational studies on polycrystals provide insight into the behavior of an evolving GB network under different driving forces. A recent study has suggested that different external stimuli (i.e. temperature and/or mechanical loading) can lead to varying degrees of GB mobility enhancement [19]. *Ex situ* experiments on polycrystals are useful in determining if GB migration occurs by comparing the pre- and post-microstructure and grain size distributions and have been conducted for a variety of materials across large ranges of temperatures and strain rates [2,3,34]. A recent study on nano-grained Cu suggests that Schmid factor has an impact on stress-assisted grain growth [35]. This study reported that grains with a favorable orientation for dislocation slip (high Schmid factor) tend to grow at the expense of less-favorably oriented grains during tensile tests to 10 % uniform strain under a relatively high strain rate ($10^{-3}s^{-1}$) (i.e. large driving force). Additional studies on gradient-structured specimens have indicated that there is a grain size for optimal grain-coarsening ability and that grain sizes above or below this value experience minimal grain size change [36]. However, these *ex situ* studies are limited in the ability to observe the GB migration mechanisms or velocity of migration in real-time [37]. In situ TEM experiments coupled with microstructure characterization are required to uncover the relationship between microstructural factors and GB behavior under loading conditions. Rottmann *et al.* combined orientation mapping with in situ TEM straining on annealed Cu (average grain size: 57 nm) and determined that wide range of GB undergo migration but found no correlation between GB misorientation angle and mobility with the exception of highly mobile incoherent Σ3 boundaries [11].

This paper presents a comprehensive investigation on the effects of different microstructural features (grain size, GB character, Schmid factor, and the effect of the loading direction) on mechanically-induced GB migration in as-deposited and annealed UFG Au thin films. We combine orientation mapping with in situ TEM nanomechanical testing and complementary MD simulations to establish statistical correlations between microstructural features and GB migration susceptibility and provide atomistic details accompanying the grain GB processes.

2. Material and methods

2.1. Experimental

Tensile specimens were fabricated in a cleanroom facility using a process involving optical lithography, electron beam (e-beam) evaporation, followed by lift-off and XeF_2 etching of the Si substrate to reveal free-stranding specimens [38]. The e-beam evaporation of Au was performed at a deposition rate of 0.5 $\AA$/s to a final thickness of 100 nm. A subset of specimens were then annealed at 350 °C for 30 min in vacuum (20 mTorr).

In situ TEM straining experiments were conducted using a custom built microelectromechanical system (MEMS) device that has been previously used to study similar specimens [39–42]. The components of the device include a thermal actuator, two capacitive sensors, a load sensor beam, and the specimen gap. When a voltage is applied across the actuator, resistive heating causes the thermal actuator to shift the central shuttle by a displacement X_A. This shift in the central shuttle causes a shift in the first capacitive sensor (CS_1) which results in a change in capacitance. From this capacitance change, the displacement X_A can be calculated (see Refs. [39,41] for more details on MEMS operation). A specimen is placed across the specimen gap, connecting the thermal actuator/CS_1 portion of the MEMS to the second capacitive sensor CS_2. This capacitive sensor is rigidly connected to the load sensor beam and allows for the measurement of the displacement of the load sensor X_{LS}. From these displacements, the displacement of the specimen can be determined as $X_S = X_A - X_{LS}$. The force F can be determined by considering the known stiffness of the load sensor beam (K_{LS}) and X_{LS} following: $F = K_{LS}X_{LS}$. The stress on the specimen can then be determined by considering the specimen geometry (nominal gauge width ~1.75 μm and 100 nm-thick). Each specimen is individually placed onto the MEMS using a micromanipulator under a light microscope and clamped using UV curable glue. The specimens are far enough from the actuator that no significant temperature increase of the specimens is expected [43].

Prior to straining, procession electron diffraction (PED) was performed on a ThermoFisher Tecnai F20 TEM operating at 200 kV at the University of Alabama. The step size was 5–10 nm with 2–3 processions, depending on the grain size. The orientation map was analyzed using Orientation Imaging Microscopy (OIM) software. The data were cleaned using confidence index standardization (minimum grain size of 5 and 7° tolerance angle) followed by grain dilation restricted to points with a confidence index <0.1. In situ TEM straining experiments were conducted using a ThermoFisher Tecnai F30 operating at 300 kV. Specifically, the specimens were loaded to different stress levels at which points the MEMS displacement X_A was kept constant (leading to slight stress relaxation due to time-dependent plastic deformation [38,44]) for observing GB migration. TEM images were collected at approximately one-minute intervals and combined and stabilized to form time lapse videos, enabling direct observations of the microstructure evolution during loading. The microstructural changes such as GB migration or grain growth were documented for both the as-deposited and annealed specimens and related to the initial orientation maps.

The GB migration behavior was tracked by manually tracing the grains in each collected image. This task is complicated due to the presence of bend contours, which can be difficult to differentiate from the GBs. To aid in this task, the collected images were assembled into an image stack and aligned using a consistent feature (e.g. a triple point that did not migrate). By cycling through the images, GBs, which do not reverse migration direction during strain relaxation, can be differentiated from other features such as bend contours that can undergo a range of contrast fluctuations. In addition, the initial orientation maps, when available, provided a valuable unambiguous starting point in the GB identification. It should be noted that, even with this approach, some boundaries could not be unambiguously identified and were left out of the analysis.

For one experiment on the as-received material, the microstructure was analyzed before and after deformation using 4D-STEM. This experiment was conducted in Georgia Tech's ThermoFisher Tecnai F30 microscope operated at 300 kV. The Gatan STEMx system was used to collect nanobeam diffraction patterns in a regular grid prior to deformation and after straining to yield and allowing to relax for forty minutes. The patterns were collected using a Gatan Metro 300 direct electron detector in a square grid pattern with a step size of ~6.8 nm and using an approximated convergence angle of 1.2 mrad. The patterns were analyzed using the STEMx OIM package for DigitalMicrograph. This package relies on a template matching approach similar to that developed by Rauch and Veron to determine the local crystallographic orientation [45]. To increase the diffraction pattern contrast, neighbor pattern averaging and reindexing (NPAR) was applied using the same approach as has been developed for electron backscatter diffraction (EBSD) analysis [46]. Maps were generated and the data were analyzed using OIM software. Grains that contained fewer than 5 pixels were filtered out when creating the orientation maps and grain size histograms as these were not reliably identified by the indexing.

2.2. MD simulations

MD simulations of uniaxial tension of NC Au thin films were performed using LAMMPS [47]. The initial polycrystalline structure consisted of four hexagon-shaped grains with a side length of approximately 20 nm. To investigate GB migration between grains of different sizes, a smaller grain with a side length of approximately 10 nm was embedded in each simulated film. The grain orientations along the z-axis were set to be [111] and in-plane grain orientations were random, representing the [111] texture. As a result, all GBs were of the [111] tilt type. Periodic boundary conditions were applied along the in-plane directions, and traction-free boundary conditions were applied along the out-of-plane direction. The thin film structure has dimensions of 60 × 60 × 15 nm and contains a total of 3,162,955 atoms. The interactions between Au atoms were modeled using an embedded atom method (EAM) potential [48]. To relax the GB structure, the system was annealed under zero stress by first heating to 900 K for 10 ps, then cooling to 300 K, and finally equilibrating at 300 K for 10 ps. Uniaxial tensile and compressive strains up to 10 % were applied with a strain rate of 10^8 s^{-1} at 300 K.

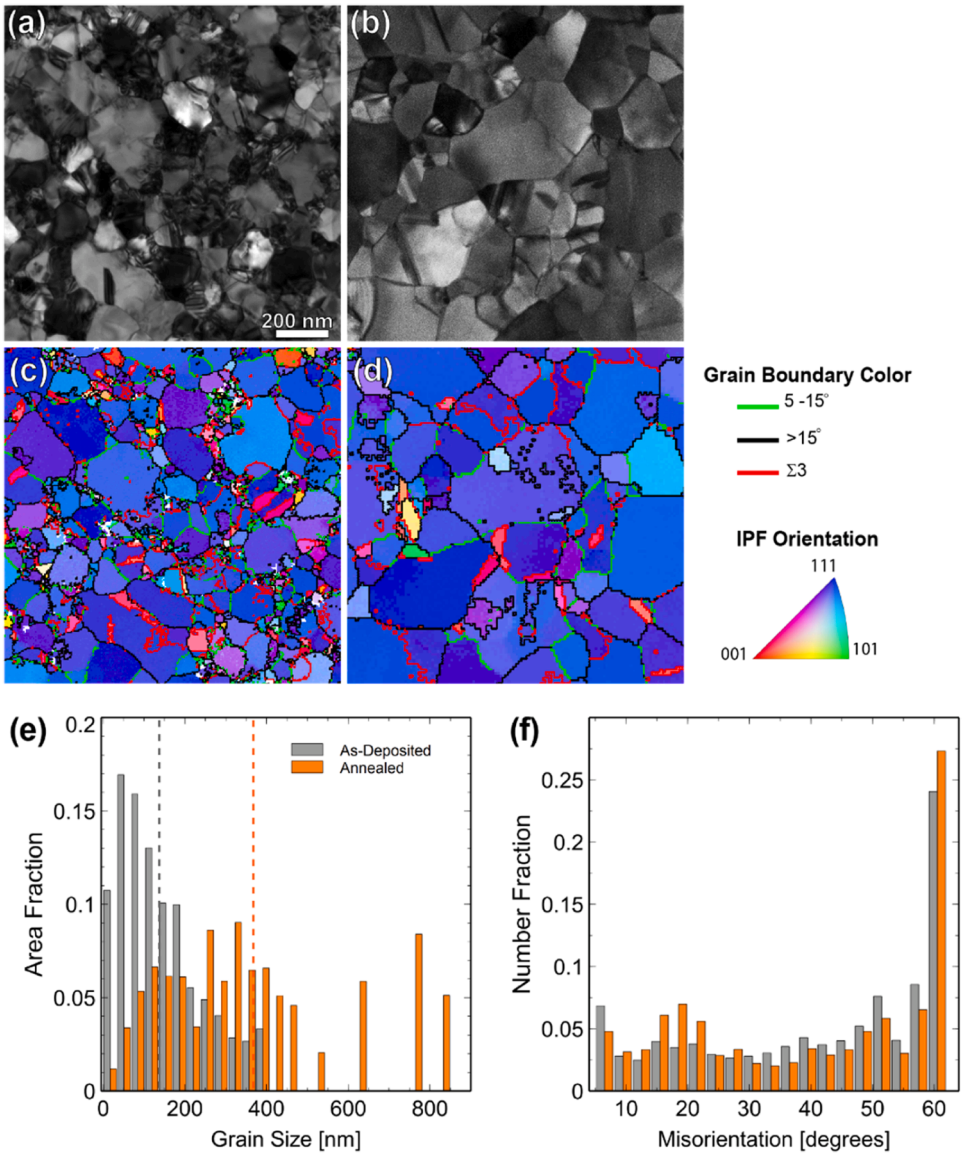

Fig. 1. TEM images of initial microstructure of (a) as-deposited and (b) annealed Au thin films with corresponding orientation map for each region in (c) and (d), respectively. (e) Area fraction grain size and (f) GB misorientation distribution for the as-deposited (grey) and annealed (orange) films. The average grain size is indicated by the vertical dashed lines and highlights the change in grain size after annealing.

3. Results

3.1. Initial Microstructure

Bright-field (BF) TEM images of the initial microstructure for the as-deposited and annealed Au specimens are shown in Fig. 1(a) and (b), respectively. The accompanying orientation map of each region is shown in Fig. 1(c) and (d). Upon annealing, the average grain size increased from 142 ± 36 nm to 360 ± 83 nm as a large portion of the small grains were removed (grain sizes determined from TEM PED dataset). The average grain sizes for both are indicated by the vertical dashed lines in the grain size distribution shown in Fig. 1(e). Specifically, 20 % of the area of the as-deposited specimens is composed of grains with sizes of 50 nm or less, whereas only 2.5 % of the area of the annealed specimen contains grains <50 nm in size. Dark-field TEM imaging suggests that, in the case of small grains, multiple through thickness grains exist (see Supplementary Information **Fig. S1**). This has important implications when considering the GB curvature as the surface GB trace, which is most visible in TEM imaging, only provides partial information on the GB morphology. Both films maintain the ⟨111⟩ dominant out-of-plane texture. Fig. 1(f) compares the GB misorientation angle θ distribution before and after annealing and shows that number fraction of GBs with $9.5^\circ < \theta < 27.5^\circ$ misorientation angle increased after annealing and those with $\theta > 30^\circ$ decreased, with the exception of twin boundaries ($\theta = 60^\circ$). In both films, a large fraction of the boundaries are Σ3 twin boundaries with the number fraction increasing slightly during annealing (0.24 to 0.27).

3.2. GB migration in as-deposited films

An example of typical GB migration/grain growth behavior in an as-deposited film is shown in Fig. 2. This experiment consisted of four stress-relaxation segments at 240, 382, 481, and 420 MPa for a total of 63 min under tension. Fig. 2(a) and (d) show BF TEM images of two different regions prior to straining. In both cases, the grain outlined by the bolded white line undergoes stress-induced grain growth in the direction of the red arrows. This resulted in the outlined grains shown in Fig. 2(b) and (e), which were taken at the end of the 3rd relaxation segment after the stress reached a maximum of 481 MPa. The initial (bolded) and final (dashed) grain outlines are overlaid on the initial orientation maps in Fig. 2(c) and (f), which facilitates easy view of the region of the microstructure that evolved during straining. In both cases, the grains expanded to absorb/remove the highly disordered regions composed of small grains in the vicinity.

A detailed analysis of the evolution of a cluster of grains during stress relaxation in an as-deposited Au film is shown in Fig. 3. This is shown to illustrate how grains are rearranged due to the disappearance and growth of certain grains. Fig. 3(a) shows a BF TEM image of the initial GB network outlined with 6 grains identified by lettering. Fig. 3(b)-(d) shows grain growth, shrinkage, and disappearance leading to a significantly different microstructure compared to the initial state. The specific changes that occur between TEM images is best seen in the outlines shown in Fig. 3(e)-(g). The grains highlighted in red in Fig. 3(e) are removed during the transition from Fig. 3(a) to (b) (dashed outline is from (a) and solid outline is from (b)). The removal of grains leads to the

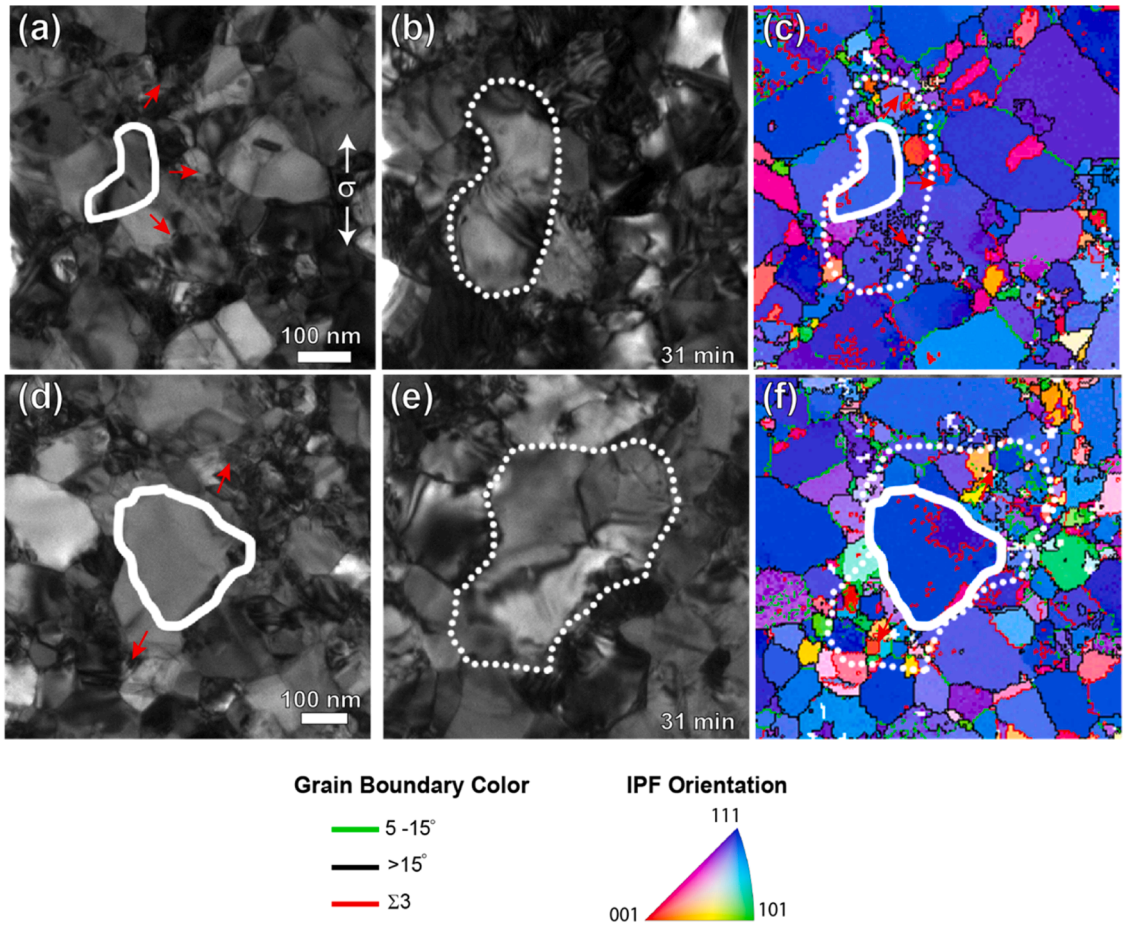

Fig. 2. Stress-induced grain growth and the removal of small grains in an as-deposited Au film. BF TEM images of (a) initial microstructure with grain traces outlined. The outlined grain undergoes extensive grain growth in the direction of the red arrows (stress is applied in the vertical direction as indicated). (b) BF TEM image taken after 31 min under a tensile load. The outline represents the final grain size/shape. (c) Corresponding orientation map of the region with the initial and final grain outline overlaid. (d)-(f) Similar analysis of a second region.

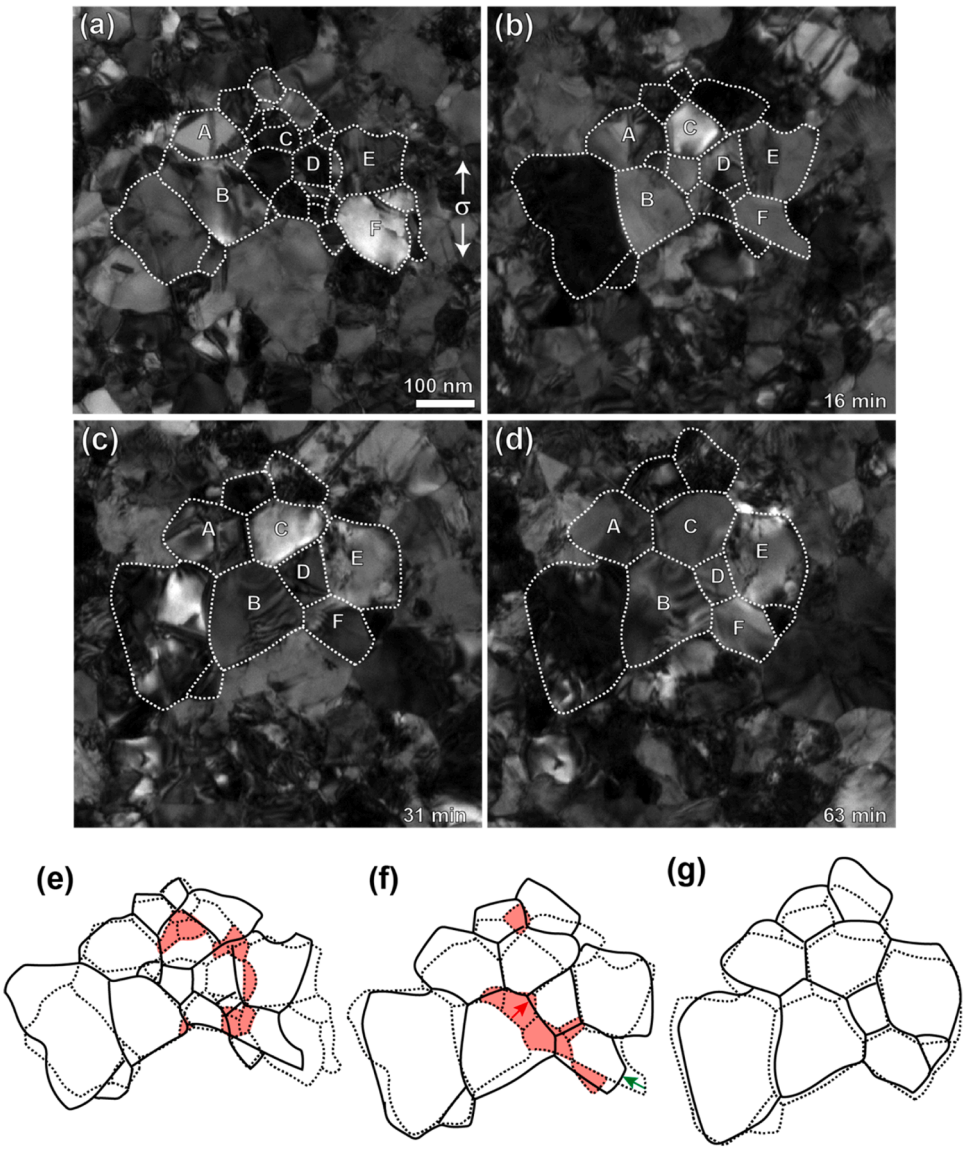

Fig. 3. Analysis of the grain growth and shrinkage of a cluster of grains. (a) Initial microstructure with GB cluster outlined and certain grains that are constant throughout the transformation identified by letters. Same region with the GB network outlined (b) 16, (c) 31, and (d) 63 min after an applied load. The grains are labeled to help identify how the grains have been rearranged. (e) Overlays of the GB network between (a) (dashed) and (b) (solid) with the grains that are removed during the transition highlighted in red. (f) Overlay of (b) (dashed) and (c) (solid). (g) Overlay of (c) (dashed) and (d) (solid) showing minimal changes for the last 32 min of the experiment.

growth of grains 'C' and 'D'. Additional grains are removed during the transition to Fig. 3(c) (overlay shown in Fig. 3(f)), primarily contributing to the growth of grain 'D'. After this point, all of the smaller grains in this region of interest have been removed, resulting in all the labeled grains being direct neighbors. During the transition to Fig. 3(d), minimal changes occur (seen in Fig. 3(g)). Overall, this represents characteristic microstructure evolution behavior in the as-deposited specimens during stress relaxation, which is consistent with our previous in situ TEM observations done without initial orientation mapping [44].

In order to obtain statistical information regarding the GB migration/grain growth, 1/3rd of the specimen gauge was analyzed in detail to identify common characteristics of the grains that grow, shrink, or completely disappear throughout the 63-minute stress-relaxation experiment. In total, 189 grains were identified and of those, 93 grains disappeared, 39 grew, 9 shrunk, and 48 grains experienced minimal changes. The initial GB network outline is shown in Fig. 4(a), where the grains are color-coded based on if the grain disappears (red), shrinks (blue), grows (green) or experiences minimal changes (grey). The white grains could not be confidently identified throughout the experiment and are omitted from the analysis. Based off this visual representation, it is clear that it is common for larger grains to grow at the expense of disappearing smaller grains as there are plenty of instances of larger green grains surrounded by smaller red grains. To further quantify this, the initial grain size for each tracked grain was recorded and used to develop a grain size distribution for the grains that grew, shrunk, and disappeared (Fig. 4(b)). This grain size distribution unambiguously demonstrates that there is a strong grain size dependence on the grain disappearance behavior. The number average grain size for the grains that disappeared was 60 ± 25 nm compared to the average initial grain size of the material of 142 ± 36 nm. The grains that grew had an average grain size of 162 ± 52 nm and those that shrunk had an average grain size of 159 ± 60 nm. The local strain within this portion of the gauge length was estimated by measuring the distance between the same edge features on the gauge which resulted in a local strain estimation of 11.7 %.

The orientation of each grain was also recorded to explore any po-

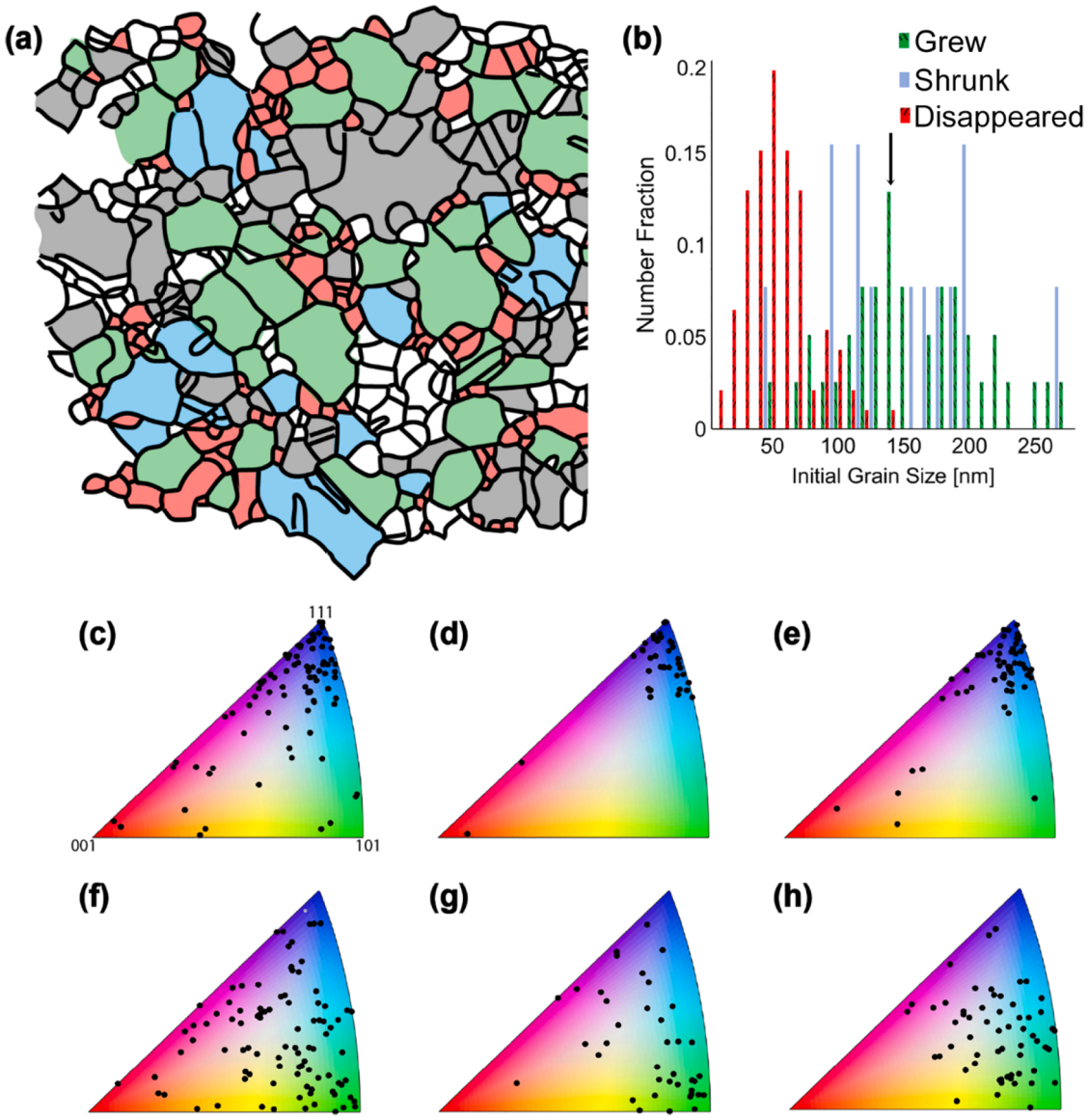

Fig. 4. Detailed analysis of grain growth and shrinkage during stress relaxation. (a) Outlined GB network with grains color coded based on if the grain disappears (red), shrinks (blue), grows (green), or undergoes minimal change (grey) throughout the 63-minute experiment. Grains colored white could not be tracked with confidence so are omitted from the analysis. (b) Distribution of grain sizes that grew, shrunk, and disappeared. The arrow indicates the initial average grain size. Out-of-plane orientation for the grains that (c) disappeared, (d) grew, and (e) experienced minimal change are plotted on IPFs, in addition to the in-plane orientation along the vertical loading direction for the grains that (f) disappeared, (g) grew, and (h) experienced minimal changes.

tential orientation dependence on the grain growth/shrinkage behavior. This is shown in Fig. 4(c)-(e) where the out-of-plane orientation for the grains that disappeared, grew, or experienced minimal changes are plotted on the inverse pole figures (IPF). A variety of grain orientations were documented for the grains that disappeared (Fig. 4(c)), including grains with orientations differing from the ⟨111⟩ film texture. There is less orientation variation for the grains that grew (Fig. 4(d)) with the majority of grains exhibiting close to the ⟨111⟩ orientation. Finally, the orientation for the grains that experienced minimal changes is shown in Fig. 4(e) and shows slight variation from the preferred ⟨111⟩ orientation. The variation in the in-plane orientation along the loading direction was also investigated and is shown in Fig. 4(f)-(h) for the grains that (f) grew, (g) shrunk and (h) experienced minimal changes. These results indicate that there is not a strong dependency on in-plane orientation with respect to the loading axis. It is important to note that in general, there is a larger variation in orientation within the smaller grains ($d < 50$ nm) compared to grains with $d > 50$ nm that tend to exhibit the dominant ⟨111⟩ orientation (see Supplementary Information Figure S2).

The crystallographic orientations were used to investigated the influence of Schmid Factor m on grain growth behavior (here the Schmid factor is calculated assuming the typical {111} slip planes for FCC materials). However, there was no significant difference in the average Schmid Factor m for the grains that disappear ($m_{avg} = 0.458 \pm 0.03$) compared to the grains that grew ($m_{avg} = 0.459 \pm 0.04$), indicating that the grain orientation with respect to favorable slip does not have a large effect on the grain growth behavior.

Collecting orientation maps pre- and post-deformation provided additional statistical analysis on the removal of small grains from the microstructure. Fig. 5(a) and (b) shows orientation maps collected and analyzed using the Gatan STEMx system prior to deformation (Fig. 5(a)) and after loading to yield and allowing to relax for forty minutes (Fig. 5 (b)). Areas highlighted in the orientation maps show the removal of clusters of small grains (roughly defined as sub-100 nm diameter) and the associated growth of larger grains. This information is quantitatively shown using an area fraction histogram constructed from the orientation

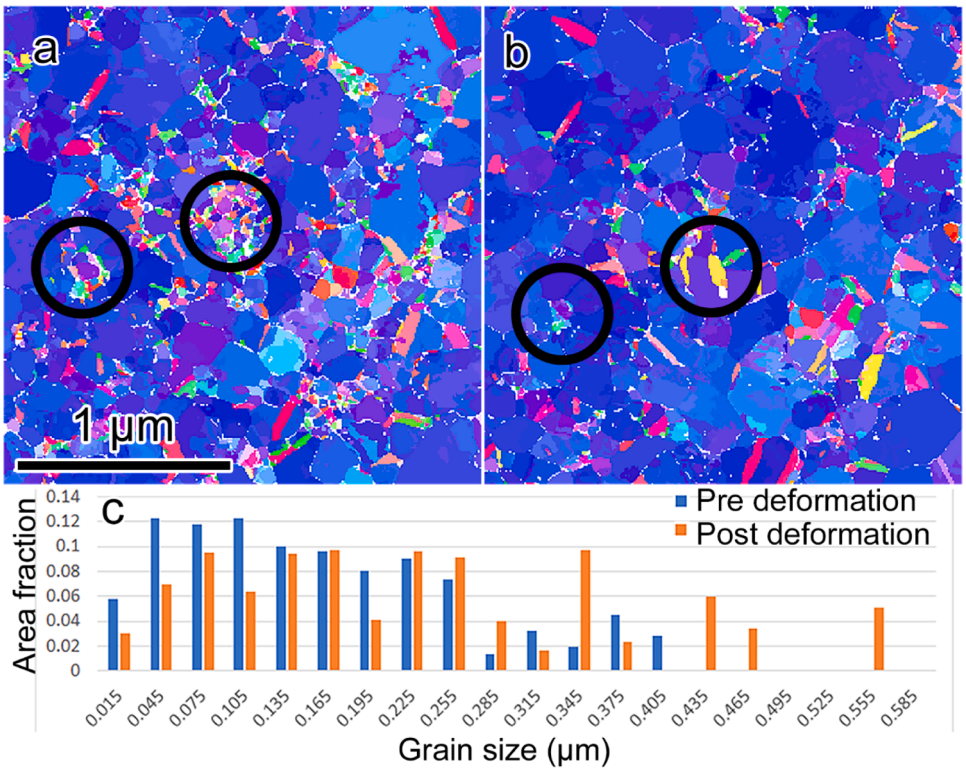

Fig. 5. Orientation maps collected a) pre and b) post deformation. Circles show regions for comparison. c) Histogram comparing the area fraction grain size pre and post deformation. Area fraction was selected to reduce the effects of spurious points on the analysis.

maps (Fig. 5(c)). The area fraction of small (<100 nm) grains decreased from 42 % pre-deformation to 26 % post-deformation and relaxation.

3.3. GB migration in annealed films

The annealed Au films are ideally suited to study migration behavior of the GB network in terms of characteristics of the GB, since there are in general fewer GBs to track and the smallest grains ($d < 50$ nm) are absent. Unlike the unannealed films previously analyzed, the GB migration is not dominated by the removal of the smaller grains since many of these grains are removed during the annealing process. An experiment was completed in which two consecutive stress-relaxation experiments were performed on an annealed Au specimen as TEM images were captured every minute. The first test consisted of 5 relaxation segments for a total time under tension of 35 mins and the second test had one relaxation for 12 min total until the specimen failed, with the stress ranging from 260 – 350 MPa.

Two examples of characteristic migration behavior in the annealed film are shown in Fig. 6. The initial microstructure, shown in Fig. 6(a), undergoes minimal changes throughout the 47-minute under tension resulting in the microstructure shown in Fig. 6(b). The orientation map of the region (Fig. 6(c)) indicates that the large grain in Fig. 6(a) contains Σ3 twin boundaries (red) that are not directly obvious based only on the TEM images. During this process, three small grains are removed and two GBs migrate as identified by the black and red arrows in Fig. 6 (c), respectively. This is further shown in Fig. 6(d), which displays the initial outline (dashed) and the final outline (solid) with the removed grains highlighted red. The GB labeled '1′ migrated a total distance of 28 nm and GB '2' migrated a distance varying from 8 to 28 nm with the migration distance of the boundary increasing near the regions where the small grains were removed.

The above analysis was completed for 1/3rd of the specimen gauge length of the same specimen to identify the migration distance for every GB possible. The results of this can be seen in Fig. 7 where the initial GB

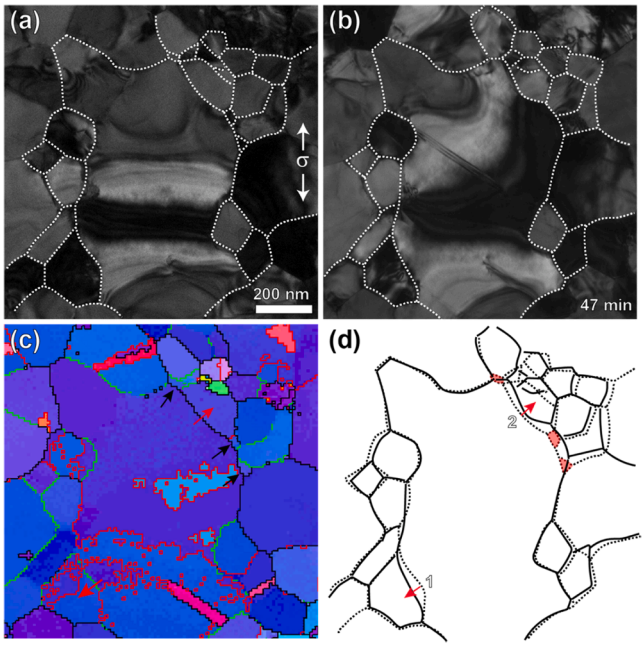

Fig. 6. GB migration in an annealed Au film. (a) BF TEM image of the initial microstructure with the GB network outlined. (b) Same region after 47 min under load. The GB network is outlined to make it visualization easier. (c) Orientation map of the same region. Red arrows indicate direction of GB migration and black arrow point to small grains that disappear. (d) Overlaid outline from (a) (dashed) and (b) (solid) to show the instances of GB migration (red arrows) and grain removal (red highlighted grains).

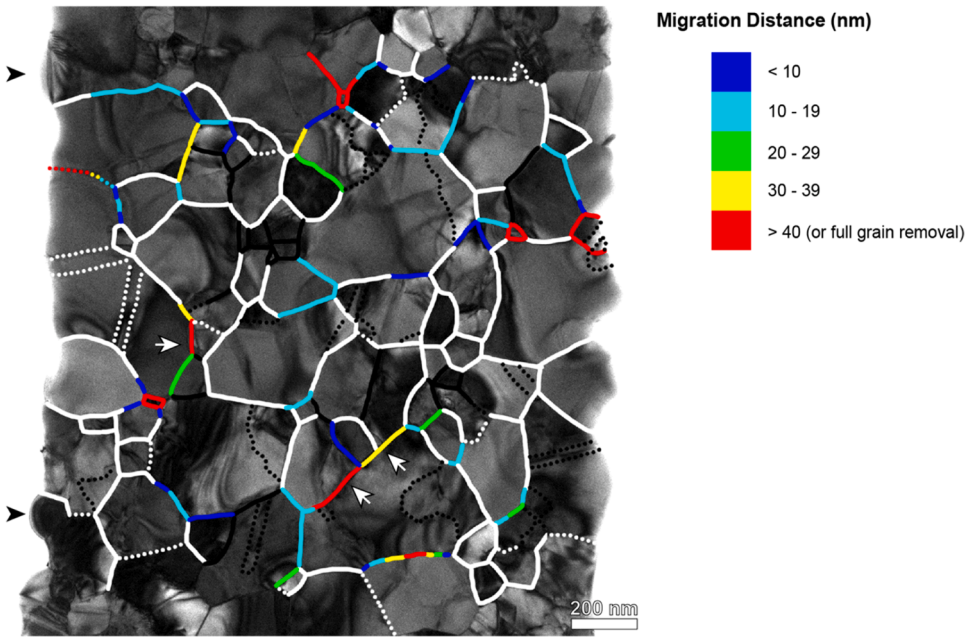

Fig. 7. GB migration distances in an annealed specimen during stress-relaxation. The initial GB network is outlined and color coded based off of the migration distance. Color legend is provided on the figure. The white boundaries did not experience measurable migration and the black boundaries could not be confidently identified so are omitted from the analysis. The dashed boundaries are identified as Σ3 twin boundaries using the orientation map. Examples of clusters of large migration distances are indicated by white arrows.

network for this section has been outlined and color-coded based off of the migration distance for each boundary. For example, the dark blue boundaries undergo minimal migration of <10 nm. The light blue, green, and yellow boundaries experience migration distances within the ranges of 10–19, 20–29, and 30–39 nm, respectively. The red boundaries migrate the most with distances greater than 40 nm, or the complete removal of a grain in cases where a full grain is outlined in red. The white boundaries undergo minimal or unmeasurable migration whereas the black boundaries cannot be confidentially identified throughout the experiment and are omitted from the analysis. The dashed GBs are Σ3 twin boundaries as identified by the orientation map of this section. One of the obvious trends from this analysis is that there tends to be clusters of larger migrations (i.e. clusters of red, yellow, and green colored boundaries). Two examples are identified by arrows in Fig. 7. This indicates that there is likely a GB connectivity effect, possibly due to the successive glide of disconnections through the GB network. Only three grains were completely removed in this gauge section during this experiment, all of which had an initial grain size $d < 75$ nm. The local strain within this section of the gauge length during the experiment was estimated to be 3.8 % (black arrowheads represent edge features used for strain estimation).

For each of the colored GBs shown in Fig. 7, the following information was identified and recorded: GB misorientation angle, GB trace angle, neighboring grain sizes, and Schmid factor. This was done to investigate the common features for mobile or immobile GBs and the corresponding migration distances. In total, 132 boundaries were tracked (66 mobile and 66 immobile). The results for the GB misorientation angle are shown below for the mobile and immobile boundaries (Fig. 8(a) and (b), respectively). Results are presented in terms of the number of mobile (or immobile) GBs for a given misorientation angle divided by the total number of GBs that were manually tracked (i.e. 132). The GB misorientation distribution for all the GBs in the specimen is shown (dashed bars) to provide context on the relative number of GBs present in the specimen for each misorientation angle (the same distribution is shown in the orange data in Fig. 1(f)). The manually tracked twin boundaries are omitted from Fig. 8(a) and (b) and shown in Fig. 8 (c) for both mobile (gray) and immobile (orange) twin boundaries. These results indicate that there is a wide range of GB misorientation angles for both mobile and immobile GBs and that there is no strong correlation between misorientation angle and GB migration. For the immobile GBs (orange), the misorientation range $32^\circ < \theta < 35^\circ$ has the largest frequency and there are three local maxima for the mobile GBs (grey) occurring at misorientation ranges of $8^\circ < \theta < 11^\circ$, $26^\circ < \theta < 29^\circ$, and $44^\circ < \theta < 47^\circ$. For the Σ3 GBs, there are variations but no distinct trends indicating correlation in the migration behavior (Fig. 8(c)). It is important to note that GB misorientation (angle and axis pair) alone does not describe the full GB structure but only defines three of the five macroscopic degrees of freedom (DOF) associated GB structure [23]. The boundary plane normal cannot be extracted from the PED data alone. This factor could contribute to the fact that no trends are observed in relation to GB misorientation angle, especially in the case of Σ3 boundaries as coherent and incoherent twins have significantly different structures.

In addition to GB misorientation, alternative parameters such as GB trace angle, grain size difference across a given GB, and Schmid Factor have been investigated with the results shown in the accompanying Supporting Information document. Overall, there was no correlation found between GB migration and the GB trace angle (angle defined with respect to the loading axis), grain size, or Schmid factor. This could be related to the fact that GB migration is intimately connected to the behavior of the TJ network. The motion of TJs can be viewed to be a result of the reaction between the disconnection glide within the three GBs that join to form the TJ [23]. If TJs inhibit disconnection glide through the network (leading to accumulation), this can result in back stress on the GB disconnections, leading to GB migration stagnation. If the GB disconnections are compatible with one or more of the connecting GBs, disconnections can flow through and lead to the connectivity effects observed in Fig. 7. A specific example of the GB network effect is shown in Fig. 9 (Supporting Movie 1). Fig. 9(a) shows the initial microstructure of the grains/GB network with the GB labels provided in Fig. 9(e). Disconnections are emitted from the TJ (marked by arrowhead) and glide in the direction of the red arrow along the boundary planes GB_{1-3} (evidenced by the flickering of contrast along this GB in Supporting Movie 1). There is also evidence that disconnections glide

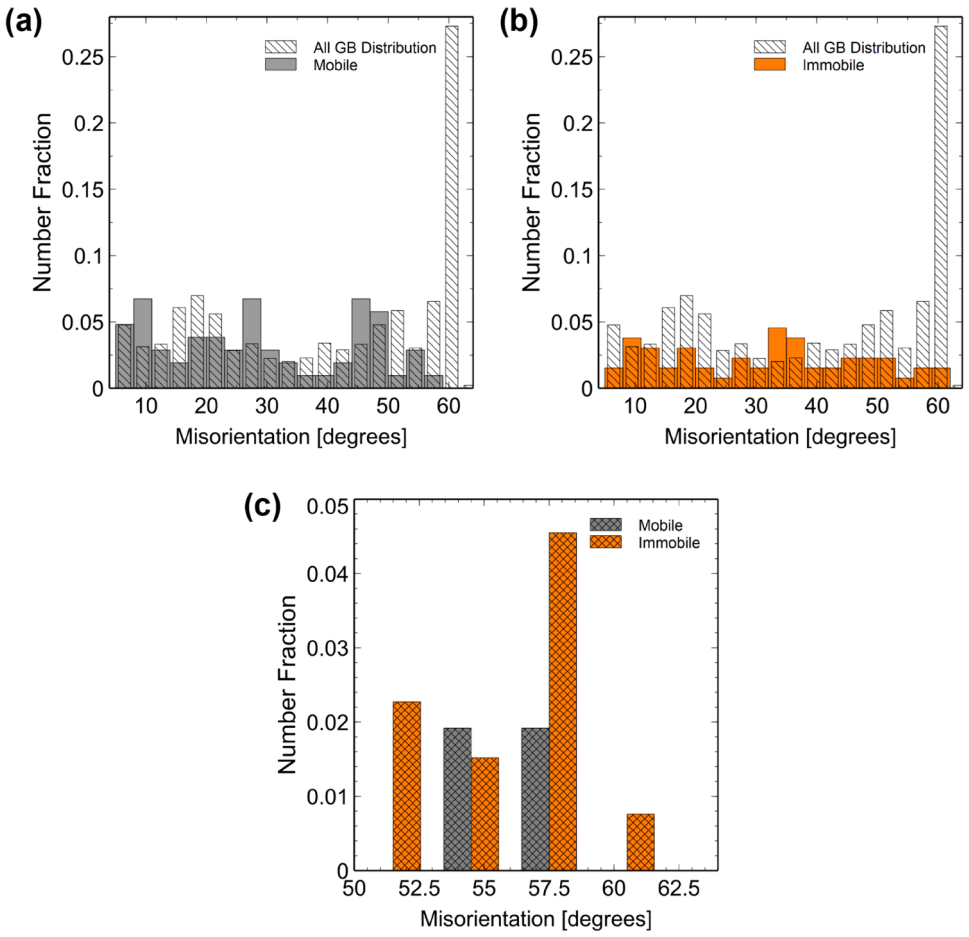

Fig. 8. GB misorientation angle distribution for (a) mobile and (b) immobile GBs during the stress-relaxation segment. Number fraction is given in terms of the fraction of GBs for a given misorientation angle that are mobile or immobile compared to the total number of GBs that were manually tracked during the experiment. The GB distribution for the full specimen is shown on each with the dashed bars (same distribution is shown in Fig. 1(f)). (c) Distribution of the tracked twin boundaries for both mobile (gray) and immobile (orange) twin boundaries.

along GB_{1-4} following the red arrow direction. This continues and dislocation glide is visible in the location indicated by the arrowhead in Fig. 9(b). PED orientation mapping of this region indicates that these dislocations are gliding along a twin boundary (GB_{1-4}). Through this process, the TJ migrates upward 20 nm at a rate of ~ 1 Å/s, resulting in the microstructure shown in Fig. 9(d). The schematic in Fig. 9(e) shows the GB network geometry before (in black) and after (in red) over the course of the 311 s separating Fig. 9(a) and (d), making it clear that the location of the TJ and GB_{1-2} has migrated. This is a case where the GBs effectively serve as highways for disconnection and dislocation glide leading to the migration of both GB_{1-2} and a TJ, though further study is needed to conclusively identify TJ networks as a dictating factor in stress-induced GB migration behavior.

3.4. MD simulations

Our MD simulations support the TEM observations of grain growth and further uncovered the underlying atomic processes that are not directly visible through TEM. Fig. 10(a) shows the top view of a simulated NC Au thin film before loading. Five grains and their associated GBs were labeled, and then tracked during MD simulations. In Fig. 10 (a), atoms were color-coded using the common neighbor analysis in OVITO [49], allowing for a clear visualization of the initial grain geometry and GB structures. Fig. 10(b), (c), (e), and (f) present MD images at ±7.5 % strains, respectively. In this work, an atom coloring scheme was developed and utilized in deformed structures to visualize both the initial GBs (time $t = 0$, colored in white) and current ones (time t, colored in purple) in the same atomic configuration at time t, as shown in Fig. 10(b), (c), (e), and (f).

Two typical types of GB geometries were investigated in MD simulations: flat GBs between large grains (GB1–6 in Fig. 10(a) and (d)) and curved GBs between a small grain and its surrounding large grains (GB7–9 in Fig. 10(a) and (d)). For the flat GBs, coupled sliding-migration assisted by disconnections was observed in MD results, which has also been reported by others through in situ TEM and MD simulations [12, 50]. This disconnection-assisted GB migration resulted in the formation of step features and boundary roughening, as seen with GB4. The direction of coupled GB sliding-migration was reversed when the applied load was flipped from tension to compression along the horizonal direction, as shown in Fig. 10(b) and (c). The elevated migration velocity at GB4 and GB6 originated from two factors. On the one hand, the associated GB planes were inclined with the loading direction, resulting in a larger resolved shear stress on these GBs compared to GB2 and GB5. As the energy barrier for GB migration is stress dependent and can be approximately expressed as: $E(\tau) = E_0 - \tau V$, where τ is the resolved shear stress, E_0 is the athermal energy barrier at $\tau = 0$ and V is the activation volume [51,52], this elevated resolved shear stress is expected to reduce the energy barriers for coupled GB sliding-migration. On the other hand, although GB4/GB6 (12.8° misorientation angle) and GB1/GB3 (22.3° misorientation angle) have similar inclinations to the loading direction and similar τ, the higher coupled sliding-migration rates observed for GB4/GB6 suggest lower energy barriers, likely due to differences in GB structures resulting from variations in GB misorienation and inclination.

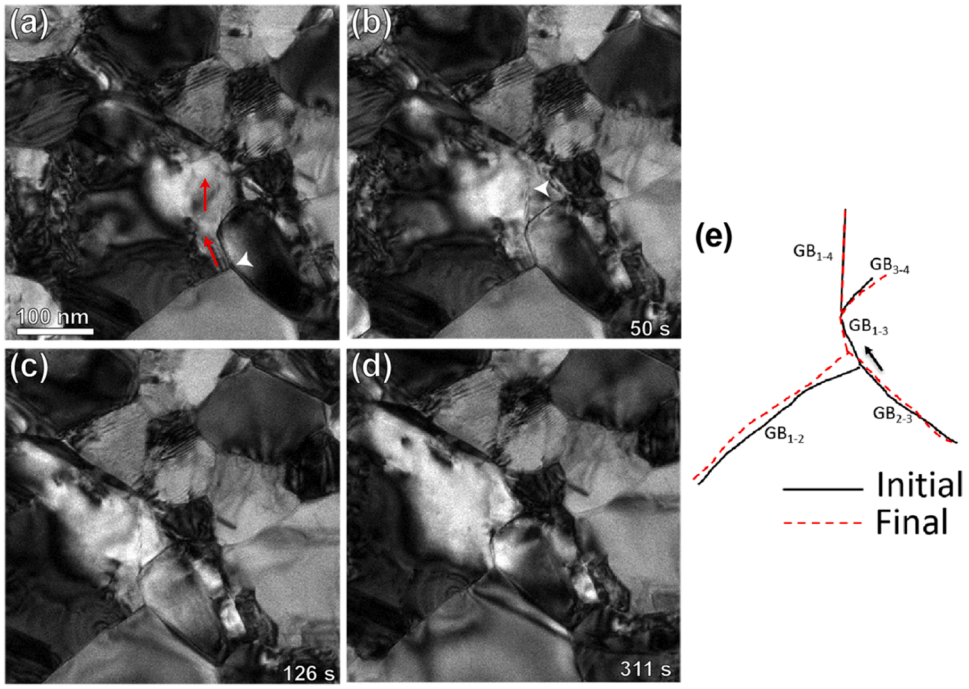

Fig. 9. An example of GB network effects where intergranular dislocation glide leads to triple junction migration during stress-relaxation. (a) intergranular dislocation glide on two GBs (direction of both indicated by red arrows). The white arrowhead marks the triple point that undergoes migration throughout the series of TEM images. (b)-(d) continued intergranular dislocation glide resulting in migration of TJ. White arrowhead in (b) marks visible dislocations. (e) schematic of the initial (black) and final (red dashed) trace of the GBs with arrow indicating TJ migration. Note that the initial GB location was determined via PED mapping in conjunction with the bright field TEM images.

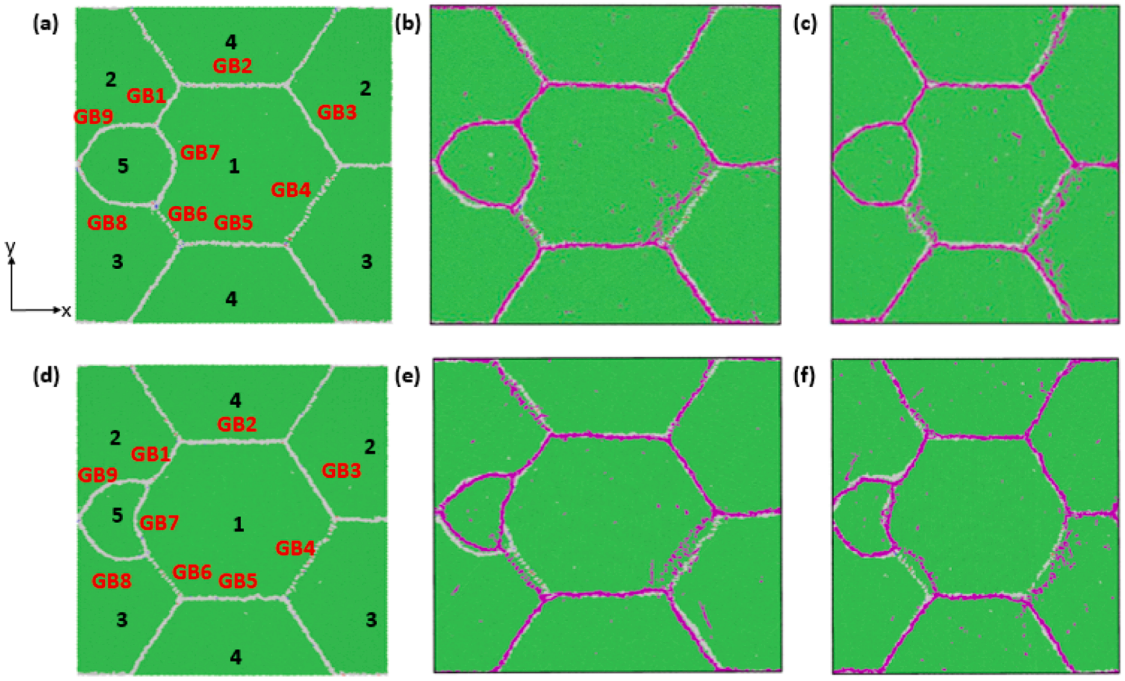

Fig. 10. MD simulations of GB migration in NC Au thin films. (a) GB structures after annealing, with the small grain (#5) having a convex GB segment. (b,c) GB structures at ±7.5 % strains, respectively. Initial GB structures are colored in white and current GB structures are colored in purple. (d) GB structures after annealing, with the small grain (#5) having a concave GB segment. (e,f) GB structures at ±7.5 % strains respectively.

Note that, as the boundaries exist within a network, the motion of the boundaries is constrained by the migration of shared TJs. This can result in local increases in the curvature of initially flat GBs during disconnection-mediated migration. This is especially evident in short GB segments such as GB6 in Fig. 10(f).

In addition to disconnection-mediated GB migration at flat GBs, curved GBs (GB7–9) were also investigated, as shown in Fig. 10(b). GB8 exhibited the most significant migration at the expense of grain 5. To reveal the role of applied stress in migration of curved GBs, the load was reversed from tension to compression, as shown in Fig. 10(c).

Correspondingly, GB7 and GB9 became more active compared to GB8 and moved towards grain 5. Despite different migration sites, initially curved GBs moved in the directions that reduced the local curvature in the MD simulations. Our analysis of the MD simulations indicate that the motion of atoms during GB migration was controlled by the sliding of GBs under applied shear stress, as schematically shown in Fig. 11(a). This process is further examined by tracking the relative atomic motion across the GB to reveal its coupled sliding-migration, as shown in Supplementary Information Fig. S6 and Supplementary Movie 2. In Fig. 11 (a), the initial GB (solid blue line) separated two neighboring grains. When a shear stress was applied, the tendency for sliding of the GB was hindered by the local curvature. Consequently, atoms in grain I on the GB were transferred to grain II through shuffling, resulting in the migration of the GB towards grain II (indicated by the blue arrow) and accordingly a reduction in local curvature. This process was repeated at GBs of small grains, which usually exhibited a positive curvature, resulting in continuous GB migration at the expense of small grains, as observed in experiments. Our MD simulation also captured this phenomenon at GB7 during tensile loading, as shown in Fig. 11(c) and (d). Specifically, an atom in the first atomic layer of grain 5 next to the GB was tracked and colored in red (Fig. 11(c)). During tensile loading, this atom was transferred to the first atomic layer of grain 8 through shuffling at 3 % strain, as shown in Fig. 11(d). As a result, GB8 migrated at the expense of grain 5, and the local curvature was reduced. Our MD simulations of concave GBs further supported the above mode of GB migration, as shown in Fig. 10(e) and (f). GB7 moved toward the direction of reducing local curvature during both tensile and compressive loading.

3. Discussion

This study provides a comprehensive investigation into different microstructural features that may influence the behavior and extent of stress-assisted GB migration. This has been done by obtaining orientation maps followed by detailed analysis of in situ TEM observations made during stress-relaxation for both as-deposited and annealed UFG Au thin films.

In the as-deposited films, GB migration appears to be largely dominated by the removal of the small grains ($d < 50$ nm). This is clearly seen through the TEM documentation of the microstructure during stress relaxation (Fig. 2 and Fig. 3). Quantitative support for this is shown in the grain size distribution (Fig. 4(b), Fig. 5(c)), unambiguously showing the propensity for small grain removal. These observations are consistent with other experimental [6,11] and computational studies [19] that report similar preferential removal of small grains under mechanical loading. Small grain removal is still present in the annealed films (Fig. 6). However, there are only a few occurrences due to the fact that the small grains are largely removed during annealing prior to straining.

The fact that small grains are consistently removed upon straining indicates that there is a driving force acting on the small grains simultaneous to the driving force provided by the applied stress. GB energy, or capillary forces, are known to be high for small grains since the GB curvature increases as the grain size decreases. In addition, the removal of grains from the microstructure via GB migration decreases the total GB energy, suggesting that the reduction in GB energy could be a significant driving force. While this driving force is traditionally associated with thermally-driven grain growth at elevated temperatures [53], the combination of applied stresses and drive to reduce the total GB energy could potentially be sufficient to overcome kinetic barriers to GB migration.

An alternative driving force is related to elastic anisotropy that evolves under an applied stress. The stored elastic strain energy density varies across different grains at the same applied load [26,54]. Under this driving force, GB migration will occur towards the grain with the larger strain energy density in attempt to decrease the overall energy of the system. This driving force has two contributing factors: grain orientation and grain size. Since the elastic modulus is dependent on the grain orientation, grains will have different stored elastic energy densities based solely on their orientation. If this was a primary factor in controlling GB migration/grain growth in these films, one would expect

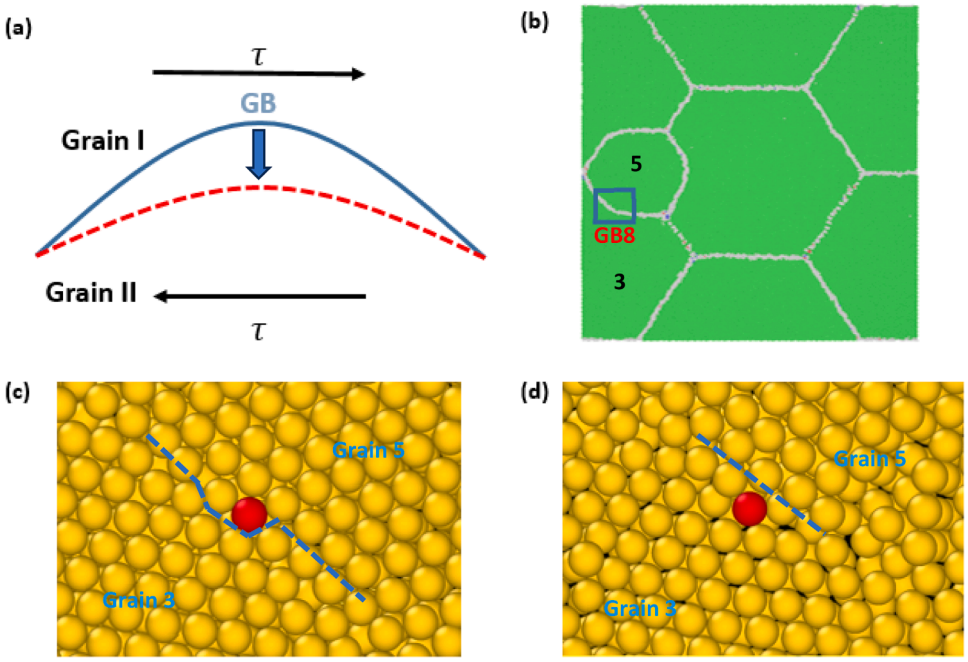

Fig. 11. MD analysis of GB migration in a thin film of NC Au. (a) Schematic of migration of a curved GB from its initial position (blue solid line) to a new position (red dashed line) under applied shear stress τ. The direction of GB migration is indicated by the blue arrow. (b-d) Tracking of a unit process of GB migration at the curved GB8 during tensile loading of the same simulation sample as in Fig. 9(a). The blue boxed region in (b) is magnified in (c) before loading and (d) after loading. (c) Atomic configuration before loading. An atom (colored in red) in the first atomic layer of grain 5 next to the curved GB8 is tracked during tensile loading. (d) Corresponding atomic configuration after loading, showing that the tracked atom is shuffled to the first atomic layer of grain 3 next to the curved GB8.

to see grains of certain preferred orientations grow or shrink. For example, a recent study has reported that a < 100> texture develops in fatigue-tested UFG Ni due to the preferential growth of ⟨100⟩ grains during high cycle loading. Despite the low driving forces for grain growth at the low strain amplitude level (<0.3 %), the high number of load cycles led to a cumulative effect of grain growth. The authors attributed the texture development due to the <100> orientation having the smallest effective elastic constants and thus the smallest strain energy density [16]. This is also consistent with other studies that report texture development from mechanical loading [18,35]. Analyzing the orientation of the individual grains that grew/shrunk (Fig. 4(c)-(h)) illustrates that this is not the case in this study. Although there is a larger variation in the orientations for the grains that were removed in Fig. 4 (c), there does not appear to be a strong preferred orientation for grains that disappear versus grains that grow. In addition, there was no relationship between the in-plane grain orientation along the loading axis which further suggest that elastic anisotropy is not a contributing factor to the observed grain growth/shrinkage.

Another grain-to-grain variation in strain energy density arises from grain size dependent yielding (Hall-Petch effect) [1]. Under an applied stress, each grain deforms elastically until the larger grains will yield through dislocation generation and slip. This yielding occurs at a lower stress level than the yield stress required in the smaller grains and as a result, the elastic strain energy density within the larger grains is smaller than that of the smaller grains. This results in a difference in strain energy density across a GB and can promote GB migration towards the small grain and eventually lead to the complete removal of small grains. This can explain the rapid and extensive small grain removal observed in the as-deposited films after a stress is applied. This has previously been proposed as a dominant driving force for small grain removal under cyclic loading [6], but these results indicate that this is likely a strong driving force under monotonic loading conditions as well. The in situ deformation experiments showed significant dislocation activity in the larger grains (Fig. 8) and no observable dislocation activity in the smallest grains. While the absence of an observation does not prove that dislocation activity was non-existent in the smallest grains, it does provide support for grain size-dependent yielding.

Although grain size-dependent yielding cannot be captured in MD simulations due to timescale limitations, our MD simulations revealed the processes of GB migration at the expense of small grains. MD results demonstrated that GB sliding in initially curved GBs smoothed out local curvature under applied stresses, aided by atomic shuffling. For as-deposited specimens in experiments, small grains typically exhibited positive curvature, resulting in GB migration at the expense of small grains. This local adjustment also occurred for annealed specimens and was consistent with Fig. 7, where most active GBs were flat after GB migration. The growth of large grains at the expense of thermodynamically less-stable small grains has been observed extensively under thermally-driven processes [55], including at room temperature in nanocrystalline Cu [56], often leading to abnormal grain growth. In the current study, no GB migration was observed at room temperature without an applied stress. This suggests that, while the reduction of GB length via curvature-driven growth is a factor in the observed behavior, it is insufficient without an additional driving force.

The annealed UFG Au specimens in this study provide an ideal testbed to study the behavior of stress-assisted GB migration that is not associated with small grain removal (since most of these grains were removed upon annealing). Local microstructure factors such as GB misorientation angle, GB trace angle, grain size, and Schmid factor were investigated with no single component appearing to have a clear correlation with stress-induced GB migration. For example, GBs of a wide variety of GB misorientation angles are mobile or immobile (Fig. 8), which is consistent with previous reports that there is no general correlation between mobility and GB misorientation angle in polycrystals [11,57]. There is also not a clear trend related to the GB trace angle with respect to the loading axis (Fig. S3), indicating that the direction of maximum shear does not have a large influence on GB migration. This analysis does assume that the boundaries are perfectly edge-on and, although this is true for most of the boundaries, it may be an over simplification that can influence the apparent results. Unlike the unannealed films, there is minimal impact of grain size on the grain boundry migration (Fig. S4). As mentioned previously, this is likely due to the fact that the grains are on average larger and have a more uniform strain energy density due to limited grain-size yielding. Finally, there appears to be no effect of Schmid factor on stress-induced GB migration in this study as there is no clear correlation between coarsening ability ($\Delta d/d_0$) and the Schmid factor for a given grain (Fig. S5). This could indicate that intragranular plastic deformation does not have an impact on intergranular mechanisms or that dislocation slip has less of an effect at the low levels of plastic deformation achieved in these experiments. Other studies have reported the growth of 'soft' grains (high Schmid factor) at the expense of 'hard' grains at large levels of deformation. However, this was for randomly-textured Cu with smaller grains ($d \sim 60$ nm) under a large GB migration driving force (i.e. large stress/strain at a faster applied strain rate) [35]. The Au films in this report are highly textured and have minimal variation in Schmid factor across grains. Another distinction is that the grain growth in this study occurs while the specimen deforms plastically at a very low strain rate (i.e. during the relaxation experiment). The results presented here indicate that there are no observed trends under low driving forces, unlike other studies where larger driving forces are applied.

The difference in GB migration behavior between the as-deposited and annealed specimens indicates that there are likely two competing driving forces for the observed stress-induced GB migration/grain growth: 1) the strain energy difference, local GB curvature, or energy reduction through elimination of GBs that favors the elimination of small grains and 2) GB migration via stress-driven disconnection motion. The first driving force appears to only be active when there are small grains ($d < 100$nm) and differentiating between the competing mechanisms is a subject of ongoing research. The second driving force leads to network TJ and GB migration effects and does not have a direct correlation to the local microstructure conditions investigated in this work.

The mechanism facilitating the stress-induced GB migration is the successive motion of disconnections along the GBs, as shown in Fig. 9. It is possible that the small grain removal is facilitated by similar mechanisms, such as a rapid burst of disconnections, or it is also possible that the disappearance of small grains involves alternative mechanisms. Such mechanisms could include grain rotation followed by absorption, which has been recently proposed using MD simulations [19], or atomic shuffling, as the MD simulations in the current study suggest.

Here, it should be noted that, as with all in situ electron microscopy experiments, the electron beam can sometimes significantly impact the active mechanisms and kinetics of the observed processes. Past experiments by Stangebye et al. on the same samples as used in this study showed that the electron beam had minimal effects on the mechanical properties and measured activation volume during uniaxial tension and stress relaxation experiments [42], suggesting that the observed deformation mechanism are representative of those that would be expected without the electron beam.

4. Conclusion

Freestanding UFG Au specimens were characterized using orientation mapping and in situ TEM straining and features such as grain size, GB character, Schmid factor, and GB trace angle were analyzed in context of GB migration and grain growth behavior. For the as-deposited specimens, grain size has a clear effect on GB migration/grain growth with larger grains tending to grow at the expense of small grains. This was discussed in terms of a driving force associated with small grain removal related to thermal effects, grain size-dependent yielding, GB curvature, and stored strain energy density. Our MD simulations also

revealed a local smoothing effect due to coupled GB sliding-migration at curved GBs, consistent with experimental observations of both as-deposited and annealed specimens. There are no clear trends regarding GB migration behavior and GB character, Schmid factor, or GB trace angle (with respect to the loading axis), suggesting that there are additional, unidentified factors dictating the GB migration behavior.

CRediT authorship contribution statement

Sandra Stangebye: Writing – original draft, Validation, Investigation, Funding acquisition, Formal analysis, Conceptualization. **Kunqing Ding:** Visualization, Investigation. **Yichen Yang:** Investigation, Formal analysis. **Ting Zhu:** Writing – review & editing, Supervision. **Olivier Pierron:** Writing – review & editing, Supervision, Funding acquisition, Conceptualization. **Josh Kacher:** Writing – review & editing, Supervision, Conceptualization.

Declaration of competing interest

The authors declare that they have no known competing financial interests or personal relationships that could have appeared to influence the work reported in this paper.

Acknowledgments

This work was supported by the U.S. Department of Energy (DOE), Office of Science, Basic Energy Sciences (BES) Materials Science and Engineering (MSE) Division under Award #DE-SC0018960. S.S. is also supported by the U.S. Department of Energy (DOE) National Nuclear Security Administration (NNSA) Stewardship Science Graduate Fellowship (SSGF) program, provided under cooperative agreement number DE-NA0003960.

Supplementary materials

Supplementary material associated with this article can be found, in the online version, at doi:10.1016/j.actamat.2025.121330.

References

[1] E.O. Hall, The deformation and ageing of mild steel: II characteristics of the Lüders deformation, Proc. Phys. Soc. B 64 (1951) 747–753.
[2] D.S. Gianola, S. Van Petegem, M. Legros, S. Brandstetter, H. Van Swygenhoven, K. J. Hemker, Stress-assisted discontinuous grain growth and its effect on the deformation behavior of nanycrystalline aluminum thin films, Acta Mater. 54 (2006) 2253–2263.
[3] T.J. Rupert, D.S. Gianola, Y. Gan, K.J. Hemker, Experimental observations of stress-driven grain boundary migration, Science 326 (2009) (1979) 1686–1690.
[4] M. He, S. Samudrala, G. Kim, P. Felfer, A. Breen, J. Cairney, D. Gianola, Linking stress-driven microstructural evolution in nanocrystalline aluminium with grain boundary doping of oxygen, Nat. Commun. 7 (2016) 11225.
[5] O. Glushko, G. Dehm, Initiation and stagnation of room temperature grain coarsening in cyclically strained gold films, Acta Mater. 169 (2019) 99–108, https://doi.org/10.1016/J.ACTAMAT.2019.03.004.
[6] O. Glushko, M.J. Cordill, The driving force governing room temperature grain coarsening in thin gold films, Scr. Mater. 130 (2017) 42–45, https://doi.org/10.1016/J.SCRIPTAMAT.2016.11.012.
[7] K. Zhang, J.R. Weertman, J.A. Eastman, Rapid stress-driven grain coarsening in nanocrystalline Cu at ambient and cryogenic temperatures, Appl. Phys. Lett. 87 (2005) 061921.
[8] M. Legros, D.S. Gianola, K.J. Hemker, In situ TEM observations of fast grain-boundary motion in stressed nanocrystalline aluminum films, Acta Mater. 56 (2008) 3380–3393.
[9] M. Jin, A.M. Minor, J.W. Morris, Strain-induced coarsening in nano-grained films, Thin. Solid. Films. 515 (2007) 3202–3207.
[10] F. Tan, F. Li, Q. Fang, J. Li, H. Feng, Grain boundary migration and deformation mechanism influenced by heterogeneous precipitate, J. Mater. Sci. 56 (2021) 9458–9469, https://doi.org/10.1007/S10853-021-05843-Z/FIGURES/9.
[11] P.F. Rottmann, K.J. Hemker, Experimental quantification of mechanically induced boundary migration in nanocrystalline copper films, Acta Mater. 140 (2017) 46–55.
[12] S. Stangebye, Y. Zhang, S. Gupta, E. Hosseinian, F. Yu, C. Barr, K. Hattar, O. N. Pierron, T. Zhu, J. Kacher, Grain growth of nanocrystalline aluminum under tensile deformation: a combined in situ TEM and atomistic study, Mater (Oxf) 16 (2021) 101068, https://doi.org/10.1016/j.mtla.2021.101068.
[13] X.Z. Liao, A.R. Kilmametov, R.Z. Valiev, H. Gao, X. Li, A.K. Mukherjee, J.F. Bingert, Y.T. Zhu, High-pressure torsion-induced grain growth in electrodeposited nanocrystalline Ni, Appl. Phys. Lett. 88 (2006) 021909, https://doi.org/10.1063/1.2159088.
[14] S. Ni, Y.B. Wang, X.Z. Liao, S.N. Alhajeri, H.Q. Li, Y.H. Zhao, E.J. Lavernia, S. P. Ringer, T.G. Langdon, Y.T. Zhu, Grain growth and dislocation density evolution in a nanocrystalline Ni–Fe alloy induced by high-pressure torsion, Scr. Mater. 64 (2011) 327–330, https://doi.org/10.1016/J.SCRIPTAMAT.2010.10.027.
[15] M. Jin, A.M. Minor, E.A. Stach, J.W. Morris Jr, Direct observation of deformation-induced grain growth during nanoindentation of ultrafine-grained Al at room temperature, Acta Mater. 52 (2004) 5381–5387.
[16] A. Barrios, Y. Zhang, X. Maeder, G. Castelluccio, O. Pierron, T. Zhu, Abnormal grain growth in ultrafine grained Ni under high-cycle loading, Scr. Mater. 209 (2022) 114372, https://doi.org/10.1016/j.scriptamat.2021.114372.
[17] R.A. Meirom, D.H. Alsem, A.L. Romasco, T. Clark, R.G. Polcawich, J.S. Pulskamp, M. Dubey, R.O. Ritchie, C.L. Muhlstein, Fatigue-induced grain coarsening in nanocrystalline platinum films, Acta Mater. 59 (2011) 1141–1149, https://doi.org/10.1016/j.actamat.2010.10.047.
[18] P. Zhao, B. Chen, J. Kelleher, G. Yuan, B. Guan, X. Zhang, S. Tu, High-cycle-fatigue induced continuous grain growth in ultrafine-grained titanium, Acta Mater. 174 (2019) 29–42, https://doi.org/10.1016/j.actamat.2019.05.038.
[19] E.Y. Chen, P. Hamilton, B.L. Boyce, R. Dingreville, The heterogeneous nature of mechanically accelerated grain growth, J. Mater. Sci. (2022), https://doi.org/10.1007/S10853-022-07974-3.
[20] A. Kobler, A. Kashiwar, H. Hahn, C. Kübel, Combination of in situ straining and ACOM TEM: a novel method for analysis of plastic deformation of nanocrystalline metals, Ultramicroscopy. 128 (2013) 68–81.
[21] Y.B. Wang, B.Q. Li, M.L. Sui, S.X. Mao, Deformation-induced grain rotation and growth in nanocrystalline Ni, Appl. Phys. Lett. 92 (2008) 061921.
[22] S.L. Thomas, K. Chen, J. Han, P.K. Purohit, D.J. Srolovitz, Reconciling grain growth and shear-coupled grain boundary migration, Nat. Commun. 8 (2017) 1764, https://doi.org/10.1038/s41467-017-01889-3.
[23] J. Han, S.L. Thomas, D.J. Srolovitz, Grain-boundary kinetics: a unified approach, Prog. Mater. Sci. 98 (2018) 386–476.
[24] D.V. Bachurin, D. Weygand, P. Gumbsch, Dislocation-grain boundary interaction in ⟨1 1 1⟩ textured thin metal films, Acta Mater. 58 (2010) 5232–5241.
[25] D.L. Olmsted, E.A. Holm, S.M. Foiles, Survey of computed grain boundary properties in face-centered cubic metals — II : grain boundary mobility, Acta Mater. 57 (2009) 3704–3713.
[26] H. Zhang, M.I. Mendelev, D.J. Srolovitz, Computer simulation of the elastically driven migration of a flat grain boundary, Acta Mater. 52 (2004) 2569–2576.
[27] J.W. Cahn, Y. Mishin, A. Suzuki, Coupling grain boundary motion to shear deformation, Acta Mater. 54 (2006) 4953–4975.
[28] H. Fukutomi, T. Kamijo, Grain boundary sliding-migration of aluminum ⟨110⟩ Σ11 {113} symmetric tilt coincidence grain boundary and its interpretation based on the motion of perfect DSC dislocations, Scr. Metall. 19 (1985) 195–197.
[29] T. Gorkaya, D.A. Molodov, G. Gottstein, Stress-driven migration of symmetrical <100>tilt grain boundaries in Al bicrystals, Acta Mater. 57 (2009) 5396–5405.
[30] T. Gorkaya, K.D. Molodov, D.A. Molodov, G. Gottstein, Concurrent grain boundary motion and grain rotation under an applied stress, Acta Mater. 59 (2011) 5674–5680.
[31] D.A. Molodov, T. Gorkaya, G. Gottstein, Migration of the Σ7 tilt grain boundary in Al under an applied external stress, Scr. Mater. 65 (2011) 990–993, https://doi.org/10.1016/j.scriptamat.2011.08.030.
[32] I.A. Ovid'ko, R.Z. Valiev, Y.T. Zhu, Review on superior strength and enhanced ductility of metallic nanomaterials, Prog. Mater. Sci. 94 (2018) 462–540.
[33] K.G.F. Janssens, D. Olmsted, E.A. Holm, S.M. Foiles, S.J. Plimpton, P.M. Derlet, Computing the mobility of grain boundaries, Nat. Mater. 5 (2006) 124–127.
[34] D.S. Gianola, D.H. Warner, J.F. Molinari, K.J. Hemker, Increased strain rate sensitivity due to stress-coupled grain growth in nanocrystalline Al, Scr. Mater. 55 (2006) 649–652.
[35] J.X. Hou, X.Y. Li, K. Lu, Orientation dependence of mechanically induced grain boundary migration in nano-grained copper, J. Mater. Sci. Technol. 68 (2021) 30–34, https://doi.org/10.1016/j.jmst.2020.08.018.
[36] Y. Lin, J. Pan, Z. Luo, Y. Lu, K. Lu, Y. Li, A grain-size-dependent structure evolution in gradient-structured (GS) Ni under tension, Nano Mater Sci. 2 (2020) 39–49, https://doi.org/10.1016/j.nanoms.2019.12.004.
[37] Y. Zhang, J.A. Sharon, G.L. Hu, K.T. Ramesh, K.J. Hemker, Stress-driven grain growth in ultrafine grained Mg thin films, Scr. Mater. 68 (2013) 424–427.
[38] E. Hosseinian, O.N. Pierron, Quantitative in situ TEM tensile fatigue testing on nanocrystalline metallic ultrathin films, Nanoscale 5 (2013) 12532–12541.
[39] S. Gupta, O.N. Pierron, A MEMS tensile testing technique for measuring true activation volume and effective stress in nanocrystalline ultrathin microbeams, Microelectromech. Syst. 26 (2017) 1082–1092.
[40] S. Gupta, S. Stangebye, K. Jungjohann, B. Boyce, T. Zhu, J. Kacher, O.N. Pierron, In situ TEM measurement of activation volume in ultrafine grained gold, Nanoscale 12 (2020) 7146–7158.
[41] S. Gupta, O.N. Pierron, MEMS based nanomechanical testing method with independent electronic sensing of stress and strain, Extreme Mech. Lett. 8 (2016) 167–176.
[42] S. Stangebye, Y. Zhang, S. Gupta, T. Zhu, O. Pierron, J. Kacher, Understanding and quantifying electron beam effects during in situ TEM nanomechanical tensile testing on metal thin films, Acta Mater. 222 (2022) 117441, https://doi.org/10.1016/j.actamat.2021.117441.

[43] B. Pant, S. Choi, E.K. Baumert, B.L. Allen, S. Graham, K. Gall, O.N. Pierron, MEMS-based nanomechanics: influence of MEMS design on test temperature, Exp. Mech. 52 (2012) 607–617.
[44] S. Stangebye, K. Ding, Y. Zhang, E. Lang, K. Hattar, T. Zhu, J. Kacher, O. Pierron, Direct observation of grain-boundary-migration-assisted radiation damage healing in ultrafine grained gold under mechanical stress, Nano Lett. 23 (2023) 3282, https://doi.org/10.1021/ACS.NANOLETT.3C00180/SUPPL_FILE/NL3C00180_SI_009.AVI.
[45] E.F. Rauch, M. Véron, Automated crystal orientation and phase mapping in TEM, Mater. Charact. 98 (2014) 1–9, https://doi.org/10.1016/j.matchar.2014.08.010.
[46] S.I. Wright, M.M. Nowell, S.P. Lindeman, P.P. Camus, M. De Graef, M.A. Jackson, Introduction and comparison of new EBSD post-processing methodologies, Ultramicroscopy. 159 (2015) 81–94, https://doi.org/10.1016/j.ultramic.2015.08.001.
[47] S. Plimpton, Fast parallel algorithms for short-range molecular dynamics, J. Comput. Phys. 117 (1995) 1–19.
[48] S.M. Foiles, M.I. Baskes, M.S. Daw, Embedded-atom-method functions for the fcc metals Cu, Ag, Au, Ni, Pd, Pt, and their alloys, Phys. Rev. B 33 (1986) 7983, https://doi.org/10.1103/PhysRevB.33.7983.
[49] A. Stukowski, Visualization and analysis of atomistic simulation data with OVITO-the Open Visualization Tool, Model Simul. Mater. Sci. Eng. 18 (2010) 015012.
[50] A. Rajabzadeh, M. Legros, N. Combe, F. Mompiou, D.A. Molodov, Evidence of grain boundary dislocation step motion associated to shear-coupled grain boundary migration, Philos Mag. 93 (2013) 1299–1316.
[51] N.F. Mott, Slip at grain boundaries and grain growth in metals, Proc. Phys. Soc. 60 (1948) 391.
[52] T. Zhu, J. Li, S. Yip, Atomistic reaction pathway sampling: the nudged elastic band method and nanomechanics applications, Nano Cell Mech. (2013) 311–338, https://doi.org/10.1002/9781118482568.ch12.
[53] S.E. Babcock, R.W. Balluffi, Grain boundary kinetics-II. In situ observations of the role of grain boundary dislocations in high-angle boundary migration, Acta Metall. 37 (1989) 2367–2376, https://doi.org/10.1016/0001-6160(89)90034-5.
[54] J.M. Zhang, K.W. Xu, V. Ji, Dependence of strain energy on the grain orientations in an FCC-polycrystalline film on rigid substrate, Appl. Surf. Sci. 185 (2002) 177–182, https://doi.org/10.1016/S0169-4332(01)00586-4.
[55] J. Kacher, I.M. Robertson, M. Nowell, J. Knapp, K. Hattar, Study of rapid grain boundary migration in a nanocrystalline Ni thin film, Mater. Sci. Eng. A 528 (2011) 1628–1635, https://doi.org/10.1016/J.MSEA.2010.10.109.
[56] V.Y. Gertsman, R. Birringer, On the room-temperature grain growth in nanocrystalline copper, Scr. Metall. Mater. 30 (1994) 577–581, https://doi.org/10.1016/0956-716X(94)90432-4.
[57] J. Zhang, W. Ludwig, Y. Zhang, H.H.B. Sørensen, D.J. Rowenhorst, A. Yamanaka, P. W. Voorhees, H.F. Poulsen, Grain boundary mobilities in polycrystals, Acta Mater. 191 (2020) 211–220, https://doi.org/10.1016/J.ACTAMAT.2020.03.044.